Segregation scheme of Indium in AlGaInAs nanowire shells

Luca Francaviglia,[1] Gözde Tütüncüoglu,[1] Sara Martí-Sánchez,[2] Enrico Di Russo,[3] Simon Escobar Steinvall,[1] Jaime Segura Ruiz,[4] Heidi Potts,[1] Martin Friedl,[1] Lorenzo Rigutti,[3] Jordi Arbiol,[2, 5] and Anna Fontcuberta i Morral[1, 6, *]

[1]*Laboratoire des Matériaux Semiconducteurs, Institut des Matériaux, Ecole Polytechnique Fédérale de Lausanne, 1015 Lausanne, Switzerland*
[2]*Catalan Institute of Nanoscience and Nanotechnology (ICN2), CSIC and BIST, Campus UAB, Bellaterra, 08193 Barcelona, Catalonia, Spain*
[3]*Groupe de Physique des Matériaux, Université de Rouen, Saint Etienne du Rouvray, 76801, France*
[4]*European Synchrotron Radiation Facility, Grenoble, 38043, France*
[5]*ICREA, Pg. Lluís Companys 23, 08010 Barcelona, Catalonia, Spain*
[6]*Institute of Physics, École Polytechnique Fédérale de Lausanne, CH-1015, Switzerland*
(Dated: November 26, 2018)

Quaternary alloys enable the independent optimization of different semiconductor properties, such as the separate tuning of the bandgap and the lattice constant. Nanowire core-shell structures should allow a larger range of compositional tuning as strain can be accommodated in a more effective manner than in thin films. Still, the faceted structure of the nanowire may lead to local segregation effects. Here, we explore the incorporation of In in AlGaAs shells up to 25 %. In particular, we show the effect of In incorporation on the energy shift of the AlGaInAs single-photon emitters present in the shell. We observe a redshift up to 300 meV as a function of the group-III site fraction of In. We correlate the shift with segregation at the nanoscale. We find evidence of the segregation of the group-III elements at different positions in the nanowire, not observed before. We propose a model that takes into account the strain distribution in the nanowire shell and the adatom diffusion on the nanowire facets to explain the observations. This work provides novel insights on the segregation phenomena necessary to engineer the composition of multidinary alloys.

Introduction Quaternary alloys enable to independently tune the semiconductor lattice constant and bandgap by careful composition engineering. However, the controlled deposition of quaternary alloys with randomly distributed composition can be challenging. On one hand, miscibility gaps and diffusion may segregate the different species that compose the alloy, and limit the possible compositions [1, 2]. On the other hand, strain may build up when quaternary semiconductors epitaxially grow on substrates of different lattice constant. To avoid plastic relaxation [3, 4], the theoretical range of available compositions is significantly narrowed in real applications. Due to their reduced diameter, semiconductor nanowires (NWs) provide a suitable growth platform to minimize plastic relaxation, [5–10] permitting lattice-mismatched material combinations not achievable by planar schemes [11–14].

In this work, we explore the range in which In can be incorporated in AlGaAs shells of core-shell GaAs-AlGaAs NWs. The goal is to understand how much the emission energy of single-photon emitters, spontaneously forming in the shell, can be redshifted [15–17]. In particular, we want to dissociate the bandgap engineering from additional segregation effects that may occur due to the presence of In. Consequently, we characterize the optical emission and correlate it with the incorporation of In using several techniques at different length scales. We find that group-III elements in the shell segregate to different positions and generate regions of different bandgaps. In particular, we find consistent evidence of the In segregation in novel wedge-shaped In-rich features. We correlate these observations with the 3-fold polarity of the NW cross section and the migration of the adatoms on the NW sidewalls. In addition to the role of the crystal directions of the NW facets [18–20], we consider strain to cause the peculiar In segregation; the presence and distribution of strain are further analyzed by finite-element simulations as well as Raman and photoluminescence (PL) spectroscopy.

The material system: core-shell NWs The GaAs-AlGa(In)As core-shell NWs are grown in a high-mobility molecular-beam-epitaxy system (MBE, DCA P600). We use Si(111) substrates and self-catalyzed growth [23, 24] at a substrate temperature of 640°C. When the NWs are about 10μm long, we stop the axial growth by interrupting the Ga supply and consuming the catalyst. We then lower the substrate temperature to 460°C to promote radial growth of an AlGa(In)As shell on the NW sidewalls [25, 26]. We start with an $Al_{33}Ga_{67}As$ shell and then incorporate In without modifying the Ga or Al rates. For this, we varied the In partial pressure from 4.5 X 10^{-9} Torr to 2.5 X 10^{-7} Torr, while the Al and Ga pressures were kept constant. Unless stated, the samples are identified by the group-III site fraction of In measured through various techniques and expressed as percentage in the notation $Al_xGa_yIn_{1-x-y}As$ (Al, Ga, and In sum to 100%) : 0%, 1%, 2%, 3%, 4%, 15%, and 25%. An outer GaAs shell of 5 nm prevents the oxidation of the inner AlGa(In)As.

Previous reports show that the composition of an AlGaAs shell deposited around a GaAs NW exhibits

* anna.fontcuberta-morral@epfl.ch

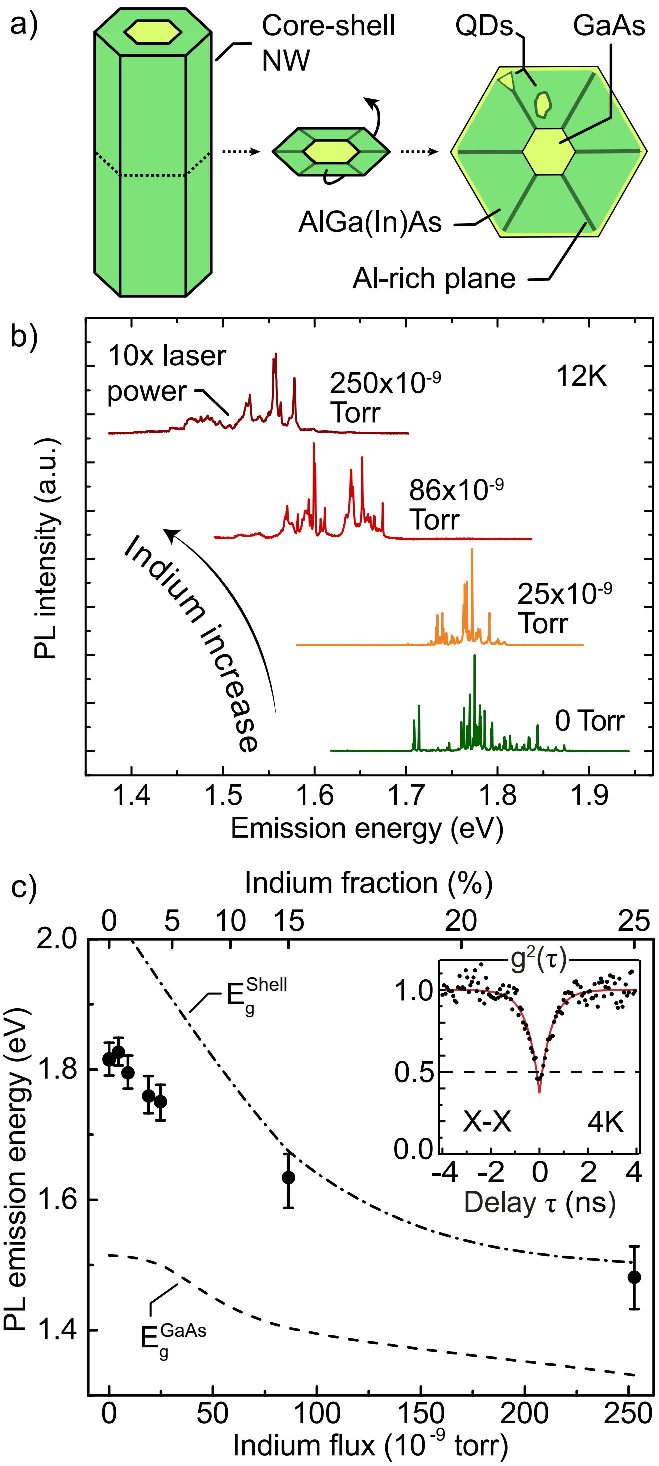

FIG. 1: (a) Sketch of a core-shell NW and shell QDs. (b) Micro-PL spectra of shell QDs grown at increasing In pressures. (c) Ensemble medians of the PL QD emission energy vs the In MBE pressure (bottom abscissa) or shell fraction (top abscissa) given by APT, XRF, STEM EDS and growth-rate calibrations. $1^{st}$and 3^{rd} quartile as error bars. The dash and the dash-dot lines are the strained core and shell bandgaps, respectively [21, 22]. Inset: single-photon g^2 of a QD exciton (3% In).

nanoscale fluctutations [15, 16, 27–30]. This phenomenon depends on the different surface mobility of Ga and Al during growth and the presence of surface-potential gradients (μ) on the NW sidewalls. The formation of Al-rich planes at the ridge between two NW facets was reported [19]. Furthermore, Ga-rich clusters can form quantum-dots (QDs) that behave as single-photon emitters in the NW shell [15, 16, 29]. A sketch of a core-shell GaAs-AlGaAs NW and its cross section is presented in figure 1a, illustrating the distribution of Al-rich planes and QDs made from Ga-rich nanoclusters.

Light-emission properties First we address the optical functionality of the core-shell NWs and embedded QDs. We used a single-frequency optically pumped semiconductor laser with a wavelength of 532 nm and power of 100 W/cm^2 focused in a spot of less than 1μm in diameter to measure NW samples at 12 K using a helium cryostat. The PL signal is collected into a spectrometer and dispersed by a 300 l/mm grating onto a Peltier-cooled CCD. The QDs in the AlGaAs shell emit bright and narrow PL lines (linewidth below 100 μeV) [15] between 1.7 eV and 1.9 eV [27]. The green spectrum at the bottom of figure 1b illustrates the PL emission of these structures; the sharp peaks are attributed to the presence of QD single-photon emitters [15, 31]. Figure 1b also contains PL spectra of the shell-QD emission for increasing In fraction, revealing several sharp peaks at different energies. The emission-energy range redshifts with increasing In fraction in the shell. One can also qualitatively determine that the QD emission linewidth broadens in samples of higher In fraction. The sample with the highest In fraction showed a decreased PL intensity, compensated for by increasing the laser power (see figure 1b).

For a statistical analysis on large ensembles of NWs and QDs, figure 1c shows the median emission energy of the QDs as a function of the measured In pressure in the MBE chamber (bottom axis) or as a function of the In fraction (top axis) measured in the shell by X-ray fluorescence (XRF) combined with atom probe tomography (APT) for 1% to 4% of In and scanning transmission electron microscopy X-ray energy-dispersive spectroscopy (STEM EDS) for 15% and 25% In (supplementary information). We measured 25 NWs from each sample. The QD emission lines were identified by an automatic routine [27]. The dash-dot line indicates the expected shell bandgap as a function of shell composition [21]. The dashed line corresponds to the GaAs bandgap. Both lines are corrected for the simulated strain [22] that arises from the core-shell lattice mismatch, as further discussed in the manuscript.

The inset in figure 1c shows a Hanbury-Brown-Twiss autocorrelation measurement ($g^2(\tau)$) of the exciton line of a QD from a sample with 3% In. The power-dependent PL showing the exciton nature of the emission line is reported in the supporting information. The sample is measured at 4.2 K in an Attodry 700 closed-cycle cryostat and is excited in continuous wave by a HeNe laser at

632.8 nm through an objective with NA = 0.81, which also collects the QD signal from the cryostat. A 1200 l/mm grating is used to select the QD line of interest that is sent to a 50:50 beam splitter. The two paths of the beam splitter are coupled to single-mode optical fibers that send the signal to two single-photon avalanche diodes, one for each path. The dip in the autocorrelation function in the inset of figure 1c is below 0.5, which is the signature of the single-photon emission. Several factors increase the count at zero delay, including background counts from QD lines spectrally close to the chosen one.

The effect of the shell-composition engineering on the QD emission energy is significant. From figure 1c, the median QD emission redshift is visible as a function of the increasing In incorporation, up to about 300 meV. In a random-distribution alloy, the addition of In to AlGaAs lowers the shell bandgap and the QD emission energy. Since these QDs form as lower-bandgap nanoscale clusters in the AlGa(In)As matrix, their emission is expected to be redshifted with respect to the shell-matrix bandgap (dash-dotted line in figure 1c). While this is true in the samples with a low In fraction (up to 4%), the median QD-emission shifts less significantly from the shell bandgap in the samples with 15% and 25% of In. Concomitantly, the overall QD emission-energy range broadens in the shells with high In fractions (figure S1 in the supplementary information and error bars in figure 1c). Together with the linewidth broadening and brightness quenching previously commented (figure 1b), these observations suggest an increasing alloy disorder as a function of the In incorporation.

Compositional analysis at the nanoscale So far, we have reported on the average In incorporation (figure 1c). In NWs the composition can vary significantly at the nanometer scale due to their faceted nature, as different facets exhibit different sticking coefficients [30]. Here we provide measurements with spatial resolution down to the atomic scale: APT and STEM-based electron energy loss spectroscopy (EELS) and EDS.

We performed laser-assisted APT measurements on the sample with 2% In. The specimen is cooled to 80 K and irradiated with UV laser light (343 nm wavelength) in 2-nJ pulses; the detection rate is 0.0025 events/pulse. The evaporated NW volume is a cylinder with diameter of 64 nm and length of 90 nm; in figures 2a - c, it is shown as a 2D projection on a plane perpendicular to the NW growth axis. Figures 2a - c show respectively the In, Al and Ga fractions. It is possible to distinguish the GaAs core by the absence of In and Al. In the shell, radial segregation of Al along the ridges between two facets of the hexagonal NW core is visible as the three Al-rich stripes in the reconstructed NW volume, in agreement with previous works [15, 16, 18, 19, 29, 30]. In addition to the Al-rich planes, APT reveals that the shell distribution of the other group-III atoms is not perfectly random. A slightly higher In fraction (up to 3%) is visible in proximity of two of the Al rich planes indicated as 1 and 3 in figure 2a. Farther from these positions, the average In fraction decreases to about 1.6%. In figure 2b and c we can also observe that the shell in proximity of the Al-rich planes is slightly depleted in Al and enriched in Ga.

To study the segregation of Al, Ga, and In in more extended regions, we studied the NW cross-sections by high angular annular dark field (HAADF) STEM and EELS in an aberration-corrected (AC) TEM microscope (FEI Titan) operated at 300 keV. We used the sample with 15% In. We prepared NW cross sections to directly map the shell composition: the NWs were spread on a Si substrate and the cross sections were FIB-cut perpendicularly to the NW growth direction (<111>). The cross-section HAADF micrographs are acquired along the <111> zone axis, with the NW sidewalls corresponding to the {110} family (figure S4 in the supporting information). Figure 2d reports the HAADF micrograph of one NW cross section. The HAADF contrast depends on the sample thickness and composition: the higher the atomic number (Z) of the species in the sample, the brighter the HAADF signal. Through high-precision FIB cut, the NW cross sections have negligible thickness variations: the contrast in figure 2d depends on the average Z at different positions across the sample. In this figure, the hexagonal shape of the NW cross section is clearly visible and the core is distinguishable from the shell. The dark stripes that form in the shell along the ridges between two NW facets ({112} crystalline directions) are due to local enrichment with a light element, such as Al, as already observed by APT and in agreement with the literature [15, 18–20]. It is possible to observe that the thickness of the Al-rich planes follows a 3-fold symmetry as observed by Zheng et al. [18]. We obtain a thickness of 3 nm and 1.7 nm for the thick and thin planes, respectively (more details in figure S4 in the supporting information). Similarly, the HAADF contrast shows that the thick planes are richer in Al than the thin ones. Comparing our observations with the literature [18], we assign the thin planes to the A polarity and the thick ones to the B polarity. Accordingly, we labelled the two polarities in figure 2d as A (orange) and B (blue).

With the exception of the Al-rich planes, the HAADF micrograph in figure 2d shows little compositional contrast in the shell. By carefully inspecting figure 2d and figure S4 in the supporting information, a slightly brighter contrast is visible in proximity of the Al-rich planes: it corresponds to a local increase in the fraction of elements with higher Z, such as Ga and In. To clarify this observation, in figures 2e - h we report the EELS maps of the upper half of the NW cross section shown in figure 2d: the selected region, indicated by the dashed rectangle in figure 2d, includes an A-polar and two B-polar ridges as well as part of the {110} NW sidewalls. The Ga, In, Al, and As distributions are shown in figure 2e, f, g, and h respectively. Principal component analysis (PCA) was used to enhance the signal-to-noise ratio in these maps [32, 33]. The NW core is clearly distinguished from the shell by the absence of Al and In and a thin Ga-rich layer, corresponding to the GaAs capping, surrounds the

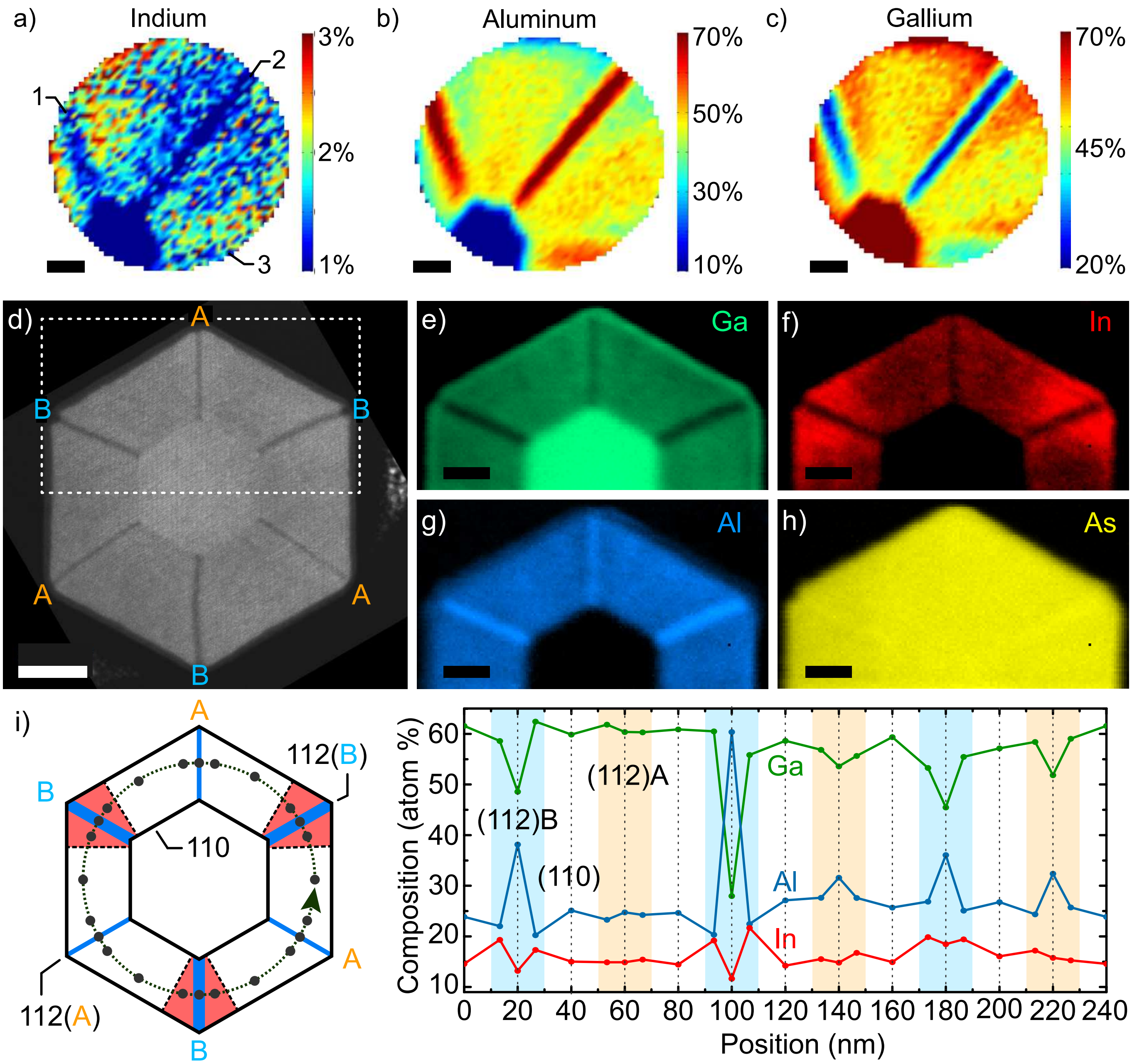

FIG. 2: (a), (b), and (c) APT of In, Al, and Ga fractions (2% In). (d) HAADF STEM micrograph of a NW cross section (15% In) with A and B polarity indicated. (e-h) EELS Ga, In, Al, and As maps of the dashed rectangle in (d). (i) Left: sketch of shell segregation. Right: shell Ga (green), Al (blue), and In (red) atomic group-III percentages vs position along the circumference in the sketch. Scale bars: (a-c) and (e-h) 10 nm, (d) 20 nm.

shell (figure 2e). As is randomly distributed throughout (figure 2f), as opposed to the distributions of the group-III elements: the presence of Al-rich planes along the hexagon ridges is confirmed (figure 2g), together with the Ga and In depletion at the same positions (figure 2e and f). Reports on GaAs-InGaAs and GaAs-InAlAs core-shell NWs [34] also show Ga and In depletion along the <112> direction. The brightness and thickness of the Al-rich planes agree with the 3-fold polarity-driven segregation previously discussed.

In agreement with the localized In enrichment shown by APT (figure 2a), STEM EELS shows in figure 2f In-rich features surrounding the Al-rich planes at the <112>B directions: interestingly, moving from the core to the outer shell, the In-rich regions become broader with a wedge-like shape on each side of the Al-rich {112}B planes. Ga has a more random distribution in the shell, although a slight increase is visible around the A-polar {112} nanofacet in figure 2e. This Ga-rich feature is not as pronounced as the In-rich ones surrounding the {112}B planes; it also has a relatively constant thickness around the {112}A planes, while the In-rich features develop an unusual wedge-shaped profile. One may also observe that, in proximity of the {112} Al-rich planes of both polarities, the Al fraction slightly decreases (figure 2g). Although the contrast is not sharp, this would agree with the local increase in the Ga and In fractions at the same positions. EELS maps on whole NW cross sections confirm the 3-fold symmetry of the shell segregation and the In enrichment only around the three <112>B directions (see the supporting information). On the left of figure 2i, a scheme summarizes the main compositional segregations observed in the NW cross sections (the scheme is aligned with figures 2d - h): the red-shaded areas indicate the wedge-shaped In-rich segregation and blue stripes indicate the alternatively thicker and thinner Al-rich planes. The polarity of the <112> nanofacets is labelled.

We acquired STEM-EDS maps of NW cross sections from the same samples as the one used for EELS. We use a FEI Tecnai Osiris TEM operated in STEM mode at 200 kV with a probe current exceeding 1 nA. The X-ray signal is collected by four silicon drift detectors under a solid angle of 0.9 srad. The NW cross sections are prepared by embedding the as-grown sample into epoxy. After hardening, the epoxy with embedded NWs is detached from the growth substrate and is mounted into an ultramicrotome and cut into 80-nm-thick slices transferred on a TEM grid. The EDS maps (figure S3 in the supplementary information) for the Ga, Al, and In distributions in the core-shell cross sections confirm the presence of the same features observed in the EELS maps. Our observations are particularly robust: three independent techniques (APT, EELS and X-ray EDS) confirm the formation of novel 3-fold wedge-shaped In-rich segregates in NWs with different average In fractions; together with the clear symmetry of these features, the agreement of the three techniques excludes artifacts due to sample preparation.

We now turn to a quantitative analysis of the distribution of the different species in the NW cross section: the EDS-based quantification is more accurate than the one based on EELS [35]. Figure 2i shows on the right a plot of the Ga (green curve), Al (blue curve), and In (red curve) atomic percentage extracted from a STEM EDS map as a function of the position along the dashed circumference shown in the sketch on the left (i.e. a circular linescan of 240nm in length). The data points at 0 nm and 240 nm correspond to the same position on the circumference (arrow in the sketch). The shaded areas are colored in orange and blue with the same coding as in figures 2g to distinguish the A- and B-polarity of the (112) directions respectively. The data points acquired in the middle of the flat {110} facets have a white background.

We focus on the most prominent fluctuation around the <112>B direction at position 100 nm. Moving from the {110} plane to the {112}B nanofacet, the Al fraction first decreases (from 25% to 20%), then rises to 60% at the corner. In smaller proportions, the In distribution is opposed to the Al trend: for the same positions, In first increases (from 14% to 19%) and then decreases to 12% at the corner. Ga is almost constant at 61% and 60% and then decreases to 28% at the corner. Very similar trends in Al/Ga/In fractions are reproduced at the six corners of the hexagonal NW cross section and are modulated according to a 3-fold symmetry: the compositional variations are consistently more pronounced in proximity of the <112>B directions.

Strain analysis and growth model We turn now to the understanding of the element distribution in the shell by taking strain into account. Figure 3a shows the PL spectra of the GaAs core at 12K for core-shell NWs of increasing In fraction. The band-edge GaAs PL redshifts from 1.51 eV down to 1.37 eV and 1.29 eV for shells containing 15% and 25% In, which we attribute to the tensile strain imposed by the shell. Tensile strain in the core is also confirmed by Raman spectroscopy (supplementary information).

To gain insight in the strain distribution imposed by the lattice-mismatched core-shell NW, we simulated the strain given the lattice mismatch, dimensions and geometry of the structure. We use the methodology of Boxberg et al. [36], adapted to hexagonal GaAs-AlGaInAs NWs at low temperature [21] in the software Nextnano [37, 38]. The strain magnitude and distributions in the core and shell are claculated by minimizing the elastic energy due to the lattice mismatch between the two. Figure 3b maps of the hydrostatic strain ϵ_{hydro} in NWs with 25% In in the shell. ϵ_{hydro} is dominated by the principal component along the NW longitudinal axis, as reported elsewhere [39]. Shear strain components are one order of magnitude smaller than ϵ_{hydro}, in agreement with previous reports [39]. As expected from the core-shell lattice mismatch, ϵ_{hydro} is on average negative in the shell (compressive) and positive in the core (tensile). We find about 2.2% of tensile strain (position "A" in figure 3b), softly modulated following a 6-fold symmetry. The shell is subject to a maximum compression of -0.35% in the middle of the NW facet (position "C" of figure 3b). The shell strain intensity is modulated by a 6-fold symmetry in a more pronounced way. The outer corners are relaxed (minimum strain of 0% at position "B" in figure 3b). Importantly, the regions of smaller strain in the shell expand around the NW sidewall ridges, becoming larger the farther they are from the core. The experimental (PL) [40] and simulated strain values are plotted in figure 3c: the simulated compressive strain in the shell (position C) and the the experimental and simulated tensile strain in the core increase linearly with the In fraction. The theoretical and experimental values agree within 15%.

A growth model that explains the non-random distribution of In and Al in the shell is presented. The expected behavior of Ga and In adatoms at the NW facets is sketched in figure 3d. We start by addressing the Al distribution. Al tends to incorporate more efficiently at the vertexes of the hexagonal cross section

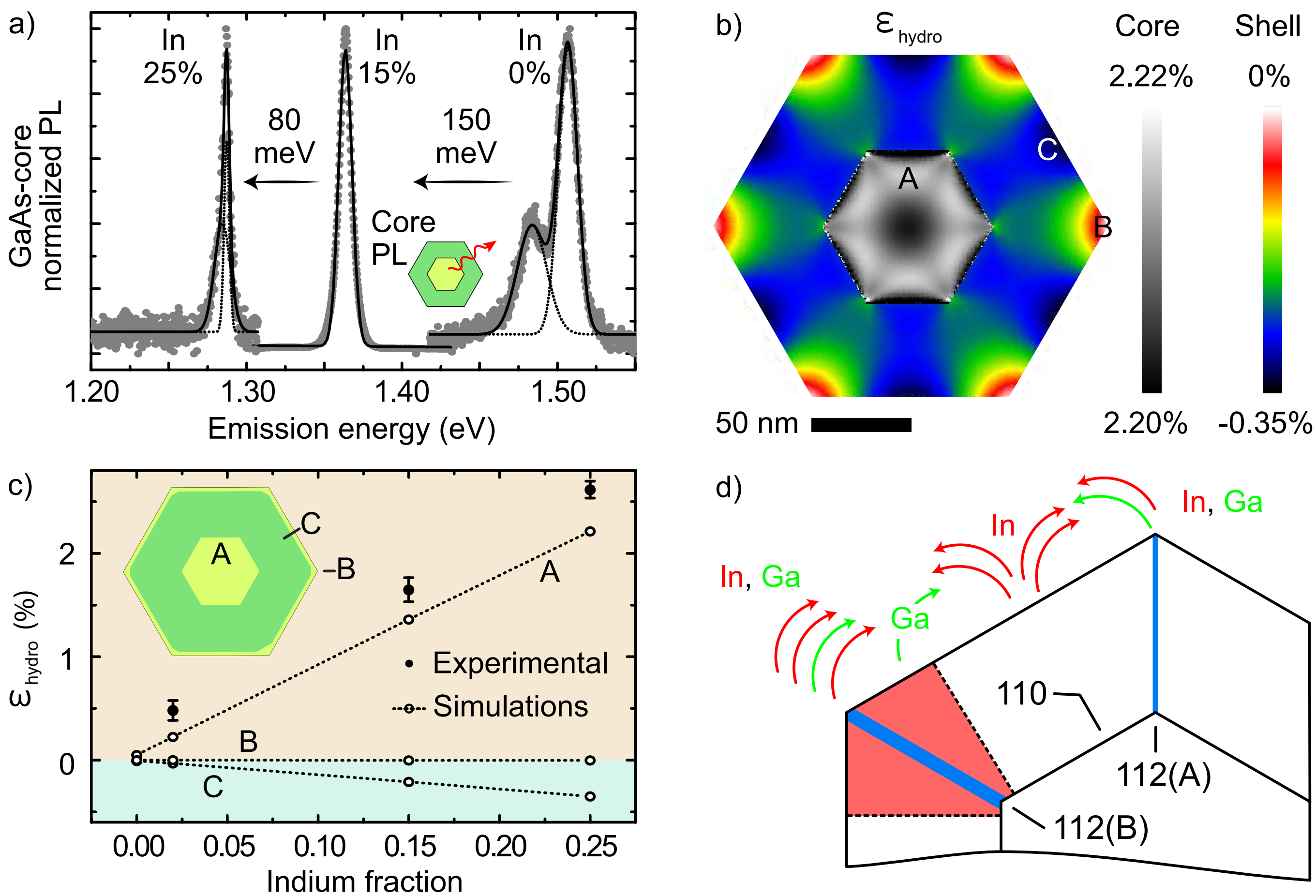

FIG. 3: (a) GaAs PL of NWs with In shell fraction of 0%, 15%, and 25%. (b) Hydrostatic strain simulation in core-shell NWs (25% In) as in ref. [36]. (e) Simulated and average experimental (1σ error bar) hydrostatic strain vs In fraction. (f) Sketch of the Ga and In diffusion on the NW sidewalls.

({112} nanofacets) [15, 18, 19]. This is the consequence of a larger sticking coefficient on those facets [41, 42]. For a similar reason, it has been shown that the incorporation is higher on B- than A-polar facets [18]. This results in a three-fold symmetry of the Al distribution.

We now turn to the incorporation of In. According to our simulations, there is a compressive strain in the middle of the facets (position C in the drawings). Since AlGaInAs exhibits a larger lattice constant than AlGaAs, we expect In to incorporate favorably in the relaxed corners. In adatoms exhibit high mobilities, allowing diffusion to occur at the scale of the NW facets. Strain relaxation should support an In flux towards the more relaxed {112} corner nanofacets, while the {110} facets exhibit a significantly lower In fraction in the centre (arrows leaving this position in figure 3d). We also observe that the In segregation seems to be enhanced by polarity. Regions with a markedly higher In fraction coincide with the {112}B vertexes. We note that the polarity-driven incorporation of In has not been demonstrated in the past. Finally, we should note that In is poorly incorporated at the highly Al-rich stripes. We attribute this to the low miscibility of In with Al-containing alloys [43]. At the {112} nanofacets In competes with Al for the available binding sites. This is particularly relevant for the (112)B-polar directions because Al tends to accumulate more in these positions.

Conclusion In conclusion, we have demonstrated a significant (300 meV) redshift of the emission energy of single-photon emitters embedded in the shell of core-shell GaAs-AlGaInAs NWs. The redshifting mechanism is based on the In incorporation in the AlGaAs shell alloy to form a quaternary semiconductor of lower bandgap. The spatial distribution of different species in the shell is determined by several high-resolution techniques of compositional analysis. In addition to the well-known Al and Ga segregation, we find evidence of novel wedge-shaped In-rich segregation. We explain the distribution of the different species in the quaternary alloy with their diffusion on the NW sidewalls driven by crystal-phase, polarity and strain. Finite-element simulations provide insight in the role of strain to drive the segregation of In. These findings advance the understating of the segregation phenomena in quaternary alloys, as required to take full advantage of the additional degrees of freedom that they offer.

Acknowledgments LF would like to thank the Nextnano team for the prompt support with the simulations and JSR the European Synchrotron Radiation Facility (ESRF) for the beamtime allocated on the beamline ID16B. LF, GT, SES, HP, MF, and AFiM thank SNF for funding through NCCR QSIT, IZLRZ2_163861 and BSCGI0_157705 and H2020 for funding through grant LIMQUET. EDR and LR thank Labex EMC3 AQURATE (French ANR). SMS acknowledges funding from "Programa Internacional de Becas "la Caixa"-Severo Ochoa". JA and SMS acknowledge funding from Generalitat de Catalunya 2017 SGR 327 and the Spanish MINECO project ENE2017-85087-C3. ICN2 acknowledges support from the Severo Ochoa Programme (MINECO, Grant no. SEV-2013-0295) and is funded by the CERCA Programme / Generalitat de Catalunya. Part of the present work has been performed in the framework of Universitat Autònoma de Barcelona Materials Science PhD program. Part of the HAADF-STEM microscopy was conducted in the Laboratorio de Microscopias Avanzadas at Instituto de Nanociencia de Aragon-Universidad de Zaragoza. Authors acknowledge the LMA-INA for offering access to their instruments and expertise. This work has received funding from the European Union's Horizon 2020 Research and Innovation Programme under grant agreement No. 654360 NFFA-Europe. The authors declare no financial interest.

---

[1] K. Onabe, Japanese Journal of Applied Physics **21**, L323 (1982).

[2] G. B. Stringfellow, Journal of Crystal Growth **65**, 454 (1983).

[3] J. W. MATTHEWS and A. E. BLAKESLEE, Journal of Crystal Growth **27**, 118 (1974).

[4] M. Leyer, J. Stellmach, C. Meissner, M. Pristovsek, and M. Kneissl, Journal of Crystal Growth **310**, 4913 (2008).

[5] R. B. Lewis, L. Nicolai, H. Küpers, M. Ramsteiner, A. Trampert, and L. Geelhaar, Nano Letters **17**, 136 (2017).

[6] O. Salehzadeh, K. L. Kavanagh, and S. P. Watkins, Journal of Applied Physics **114** (2013), 10.1063/1.4816460.

[7] S. Raychaudhuri and E. T. Yu, Journal of Vacuum Science & Technology B: Microelectronics and Nanometer Structures **24**, 2053 (2006).

[8] T. E. Trammell, X. Zhang, Y. Li, L. Q. Chen, and E. C. Dickey, Journal of Crystal Growth **310**, 3084 (2008).

[9] K. L. Kavanagh, Semiconductor Science and Technology **25** (2010), 10.1088/0268-1242/25/2/024006.

[10] M. De La Mata, C. Magén, P. Caroff, and J. Arbiol, Nano Letters **14**, 6614 (2014).

[11] F. Glas, Physical Review B - Condensed Matter and Materials Physics **74**, 2 (2006).

[12] F. Glas, in *Lattice Engineering* , edited by S. Wang (Taylor and Francis group, 2012) Chap. 5, pp. 189–228.

[13] T. Kuykendall, P. Ulrich, S. Aloni, and P. Yang, Nature Materials **6**, 951 (2007).

[14] M. De La Mata, R. Leturcq, S. R. Plissard, C. Rolland, C. Magén, J. Arbiol, and P. Caroff, Nano Letters **16**, 825 (2016).

[15] M. Heiss, Y. Fontana, A. Gustafsson, G. Wüst, C. Magen, D. D. O'Regan, J. W. Luo, B. Ketterer, S. Conesa-Boj, A. V. Kuhlmann, J. Houel, E. Russo-Averchi, J. R. Morante, M. Cantoni, N. Marzari, J. Arbiol, A. Zunger, R. J. Warburton, and A. i Morral, Nature Mater. **12**, 439 (2013).

[16] L. Mancini, Y. Fontana, S. Conesa-Boj, I. Blum, F. Vurpillot, L. Francaviglia, E. Russo-Averchi, M. Heiss, J. Arbiol, A. Fontcuberta I Morral, and L. Rigutti, Applied Physics Letters **105**, 243106 (2014).

[17] L. Francaviglia, Y. Fontana, and A. Fontcuberta i Morral, *Semiconductors and Semimetals* , 1st ed., Vol. 94 (Elsevier Inc., 2016) pp. 159–184.

[18] C. Zheng, J. Wong-Leung, Q. Gao, H. H. Tan, C. Jagadish, and J. Etheridge, Nano Lett. **13**, 3742 (2013).

[19] N. Sköld, J. B. Wagner, G. Karlsson, T. Hernán, W. Seifert, M.-E. Pistol, and L. Samuelson, Nano Lett. **6**, 2743 (2006).

[20] D. Rudolph, L. Schweickert, S. Morkötter, L. Hanschke, S. Hertenberger, M. Bichler, G. Koblmüller, G. Abstreiter, and J. J. Finley, New Journal of Physics **15** (2013), 10.1088/1367-2630/15/11/113032.

[21] E. H. Li, Physica E: Low-Dimensional Systems and Nanostructures **5**, 215 (2000).

[22] I. Vurgaftman, J. R. Meyer, and L. R. Ram-Mohan, Journal of Applied Physics **89**, 5815 (2001), arXiv:1206.0723.

[23] C. Colombo, D. Spirkoska, M. Frimmer, G. Abstreiter, and A. i Morral, Phys. Rev. B **77**, 155326 (2008).

[24] T. V. Hakkarainen, A. Schramm, J. Mäkelä, P. Laukkanen, and M. Guina, Nanotechnology **26**, 275301 (2015).

[25] M. Heigoldt, J. Arbiol, D. Spirkoska, J. M. Rebled, S. Conesa-Boj, G. Abstreiter, F. Peiró, J. R. Morante, and A. i Morral, J. Mater. Chem. **19**, 840 (2009).

[26] A. i Morral, D. Spirkoska, J. Arbiol, M. Heigoldt, J. R. Morante, and G. Abstreiter, Small **4**, 899 (2008).

[27] L. Francaviglia, Y. Fontana, S. Conesa-Boj, G. Ttncoglu, L. Duchne, M. B. Tanasescu, F. Matteini, and A. Fontcuberta i Morral, Applied Physics Letters **107**, 033106 (2015).

[28] L. Francaviglia, G. Tütüncüoglu, F. Matteini, and A. Fontcuberta i Morral, Nanotechnology (2018).

[29] N. Nari Jeon, B. Loitsch, S. Morkoetter, G. Abstreiter, J. Finley, H. J. Krenner, K. G., and L. J. Lauhon, ACS Nano **9**, 8335 (2015).

[30] N. Jeon, D. Ruhstorfer, M. Döblinger, S. Matich, B. Loitsch, G. Koblmueller, and L. J. Lauhon, Nano Letters , acs.nanolett.8b02104 (2018).

[31] Y. Fontana, P. Corfdir, B. Van Hattem, E. Russo-Averchi, M. Heiss, S. Sonderegger, C. Magen, J. Arbiol, R. T. Phillips, and A. i Morral, Phys. Rev. B **90**, 75307 (2014).

[32] P. Trebbia and N. Bonnet, Ultramicroscopy **34**, 165 (1990).

[33] I. Jolliffe, *Principal Component Analysis* (Springer,

2002).

[34] L. Balaghi, G. Bussone, R. Grifone, R. Hübner, J. Grenzer, and A. Krasheninnikov, arXiv:1803.10873 (2018).

[35] For the elements here considered, the EELS peaks overlap with an important background that is absent in the EDS spectra. The EELS background does not prevent the localization of the elements in the maps, but may reduce the accuracy of the quantification.

[36] F. Boxberg, N. SØndergaard, and H. Q. Xu, Advanced Materials **24**, 4692 (2012).

[37] A. Trellakis, T. Zibold, T. Andlauer, S. Birner, R. K. Smith, R. Morschl, and P. Vogl, Journal of Computational Electronics **5**, 285 (2006).

[38] S. Birner, T. Zibold, T. Andlauer, T. Kubis, M. Sabathil, A. Trellakis, and P. Vogl, IEEE TRANSACTIONS ON ELECTRON DEVICES **54**, 2137 (2007).

[39] J. Grönqvist, N. Søndergaard, F. Boxberg, T. Guhr, S. Åberg, and H. Q. Xu, Journal of Applied Physics **106** (2009), 10.1063/1.3207838.

[40] P. Pfeffer, I. Gorczyca, and W. Zawadzki, Solid State Communications **51**, 179 (1984).

[41] S. Koshiba, Y. Nakamura, M. Tsuchiya, H. Noge, H. Kano, Y. Nagamune, T. Noda, and H. Sakaki, Journal of Applied Physics **76**, 4138 (1994).

[42] Y. Kim, H. J. Joyce, Q. Gao, H. H. Tan, C. Jagadish, M. Paladugu, J. Zou, and A. A. Suvorova, Nano Letters **6**, 599 (2006).

[43] P. Ballet, J. B. Smathers, and G. J. Salamo, Applied Physics Letters **75**, 337 (1999).